
Article:
Kesserwani, G. and Liang, Q. (2012) Locally limited and fully conserved RKDG2 shallow water solutions with wetting and drying. Journal of Scientific Computing, 50 (1). 120 - 144.

https://doi.org/10.1007/s10915-011-9476-4

Locally limited and fully conserved RKDG2 shallow water solutions with wetting and drying

Georges Kesserwani, Qiuhua Liang*

School of Civil Engineering and Geosciences, Newcastle University, Newcastle upon Tyne NE1 7RU, England, UK

Abstract

This work extends a well-balanced second-order Runge-Kutta discontinuous Galerkin (RKDG2) scheme to provide *conservative* simulations for shallow flows involving wetting and drying over irregular topographies with friction effects. For this purpose, a wetting and drying technique designed originally for a finite volume (FV) scheme is improved and implemented, which includes the discretization of friction source terms via a splitting implicit integration approach. Another focus of this work is to design a fully conserved RKDG2 scheme to provide conservative solutions for both mass and momentum through a locally slope limiting process. Several steady and transient benchmark tests with/without friction effects are simulated to validate the new solver and demonstrate the effects of different slope limiting processes, i.e. globally and locally slope limiting processes.

Keywords: discontinuous Galerkin method; local slope-limiter *vs.* global slope-limiter; wetting and drying; irregular topography; friction term discretization; conservative scheme.

*Corresponding author: Tel. +44 191 2226413; fax: +44 191 2226502.
E-mails: Georges.Kesserwani@ncl.ac.uk; (G. Kesserwani) Qiuhua.Liang@ncl.ac.uk (Q. Liang)

1. Introduction

In practice, free-surface flows are commonly modelled by the shallow water equations (SWE). Accurate and conservative numerical solutions to the SWE may be obtained by a high-order discretization technique in the context of a Godunov-type method [26,48-50]. During the past few decades, finite volume (FV) Godunov-type schemes have gradually become a standard numerical tool in the computational hydraulics and a recent trend is to use them to solve the real-world shallow flow problems (see [4,6,8,9,21,22,26,36,37,40,45,54] and the references therein). In spite of all the attractive properties that a Godunov-type discretization has already owned [47,52], e.g. automatic shock-capturing, many well-suited FV schemes appear in the literature to survey important issues that must be considered for practical numerical calculations. These include treating irregular domain topography, handling moving wet/dry fronts and representing high value of bed roughness [11,12,35]. In respect of this, we are interested in the second-order schemes and the popular method of hydrostatic reconstruction reported by Audusse et al. [3]. Audusse et al.'s model pioneers a modern class of well-balanced and non-negative (in terms of water depth) FV schemes based on modified expressions to the fluxes and topographic source terms that entail extra hydrostatic pressure terms. While also considering the friction effects, Liang and Marche [35] and Liang [36] revisited the method of Audusse et al. [3] and delivered an alternative formulation in the context of a MUSCL FV scheme [49], which does not need those extra hydrostatic terms in the discretization of the fluxes and the bed slope source terms.

In the last decade, the Godunov-type methods incorporated with a Runge-Kutta (RK) discontinuous Galerkin (DG) local discretization [15,16] have been traded further in the field of hydrodynamic modelling [1,7,10,17-19,22-24,27,28,31,32,39,42,44,50,51]; due to many of their advantages compared with the traditional finite element and non-oscillatory FV methods [28,30-32,53]. However, the RKDG methods have not yet attained the same level of

robustness as the FV schemes and their application to realistic flow simulations is still in the embryonic stage [3,4,6,8,14,20,21,26,34-38,40,45,54]. In particular, the topic of treating wetting and drying over irregular topographies in the frame of an RKDG algorithm has just started to occupy the area of computational hydraulics. Among the very few existing RKDG wetting and drying strategies [7,10,17,24], most of them can only guarantee mass conservation but overlook the issue of momentum conservation [10,24]. However, allowing violation of momentum conservation is not theoretically recommended [48], and in practice, this issue is noticed to influence the accuracy and/or the well-balanced property of an RKDG scheme [10]. Furthermore, among these wetting and drying algorithms [7,10,17,24], no effort has been made to provide stable and accurate discretization to the friction source terms as in the FV methods [11,12,35,38].

Similar to the FV methods, RKDG schemes also employ slope limiters to remedy the numerical oscillations that may emerge around a discontinuous solution. However, slope limiting in an RKDG method is more troublesome than that in an FV scheme. Krivodonova et al. [29] and Qiu and Shu [41] showed that an FV slope limiter applied uncontrollably within an RKDG method may essentially deteriorate the order of accuracy for a smooth numerical solution and also bulk a discontinuous solution. This stipulates the necessity for localizing the slope limiting process, which is currently an ongoing research topic for the RKDG methods. In relation to wetting and drying over irregular topographies, it is often said that a slope limiter may induce drastic numerical instabilities [10,17]. But no factual insights are yet available.

This work therefore considers all of the above concerns while improving an FV wetting and drying technique [35] in the context of an RKDG2 scheme, which is implemented with a locally slope limiting process (RKDG2-LL). For numerical flux calculations, the non-negative (in terms of water depth) reconstruction of Riemann states

described in Liang and Marche [35] is implemented and then the interface fluxes are calculated using the HLL solver [48]. These non-negatively reconstructed Riemann states are also used to, locally and temporary, regenerate the approximating coefficients defining the RKDG2 solutions of the flow variables and topography when discretizing the bed slope source terms and calculating the fluxes in the local Gaussian points. This is actually a critical step in maintaining the well-balanced and non-negative properties of the scheme. A splitting implicit scheme [12,35] that was proposed to discretize the friction source terms in an FV scheme is further modified and extended to the current RKDG2 framework. Analytical and experimental benchmark tests are simulated to demonstrate the incapability of the globally limited RKDG2 model (denoted by RKDG2-GL) in handling certain flow conditions. Meanwhile, these test cases also validate the current RKDG2 in handling the moving wet/dry fronts over non-uniform topographies as well as revealing the benefits of using the locally limited model (referred to as RKDG2-LL) to provide more accurate and conservative predictions.

2. Improved RKDG2 shallow flow scheme

The conceptual underpinning of RKDG methods for solving the hyperbolic conservation laws is attributed to Cockburn and Shu [51] and other co-workers (see within [15,16]) and is not re-considered in this work. We directly outline a well-balanced RKDG2 scheme for solving the SWE [28] and then focus on the issues related to practical hydrodynamic modelling, i.e. wetting and drying over irregular topography, conservative slope limiting and stable discretization of friction terms.

2.1 Governing shallow water equations

Many different forms of the 1D SWE exist in the literature, e.g. [3,4,8,9,33,34]. The one expressed in terms of the free-surface elevation $\eta = h + z$ (where h denotes the water depth

and z is the topography function) and the unit-width discharge $q = hu$ (where u gives the depth-averaged velocity) is used in this work, which is written in a matrix form as [34]

$$\partial_t \mathbf{U} + \partial_x \mathbf{F} = \mathbf{S_b} + \mathbf{S_f} \tag{1}$$

in which,

$$\mathbf{U} = \begin{pmatrix} \eta \\ q \end{pmatrix},\ \mathbf{F} = \begin{pmatrix} q \\ \frac{q^2}{\eta - z} + \frac{g}{2}\left(\eta^2 - 2\eta z\right) \end{pmatrix},\ \mathbf{S_b} = \begin{pmatrix} 0 \\ -g\eta\partial_x z \end{pmatrix} \text{ and } \mathbf{S_f} = \begin{pmatrix} 0 \\ -C_f u\,|u| \end{pmatrix} \tag{2}$$

where **U** is the vector of flow variables, **F** contains the fluxes, $\mathbf{S_b}$ represents the topography source terms and $\mathbf{S_f}$ lists the friction source terms, , g is the acceleration due to gravity, $C_f = \frac{g n_M^2}{(\eta - z)^{1/3}}$ is the coefficient of bed roughness and n_M is the Manning coefficient.

2.2 Well-balanced RKDG2 framework

In solving the 1D governing equations using an RKDG2 scheme, the computational domain $[x_{\min}, x_{\max}]$ may be subdivided into N uniform cells via interface points $x_{\min} = x_{1/2} < x_{3/2} < \ldots < x_{N+1/2} = x_{\max}$ such that a random cell $I_i = [x_{i-1/2}, x_{i+1/2}]$ is centred at $x_i = ½(x_{i+1/2} + x_{i-1/2})$ and of length $\Delta x = x_{i+1/2} - x_{i-1/2}$. The well-balanced RKDG2 scheme [28] seeks a local approximate linear solution $\mathbf{U_h} = [\eta_h,\ q_h]^{\mathrm{T}}$ to (1), defined by the time-evolving average and slope coefficients ($\mathbf{U}_i^0(t)$ and $\mathbf{U}_i^1(t)$), *i.e.*

$$\mathbf{U_h}(x,t)\big|_{I_i} = \mathbf{U}_i^0(t) + \mathbf{U}_i^1(t)\frac{(x - x_i)}{\Delta x/2} \qquad \left(\forall x \in I_i\right) \tag{3}$$

Associated with the given initial conditions $\mathbf{U_0}(x) = \mathbf{U}(x,0)$, the corresponding initial coefficients are [28]

$$\mathbf{U}_i^{0,1}(0) = \tfrac{1}{2}\left(\mathbf{U_0}(x_{i+1/2}) \pm \mathbf{U_0}(x_{i-1/2})\right) \tag{4}$$

A local linear (continuous) approximation of topography with a similar structure as (3) and (4) provides automatically the well-balanced property for those simulations taking place in a fully wet domain [28,50]. Subsequently, by denoting the topography associated (scalar)

coefficients by $z_i^{0,1} = \frac{z(x_{i+1/2}) \pm z(x_{i-1/2})}{2}$, the momentum entry of the bed slope source terms can be finally expressed as

$$\partial_x z_h(x)\big|_{I_i} = \frac{z(x_{i+1/2}) - z(x_{i-1/2})}{\Delta x} = \frac{2z_i^1}{\Delta x} \tag{5}$$

The time derivative terms of the local coefficients are then approximated by

$$\begin{aligned} \partial_t \mathbf{U}_i^0 &= \mathbf{L}_i^0\left(\mathbf{U}_{i-1}^{0,1}, \mathbf{U}_i^{0,1}, \mathbf{U}_{i+1}^{0,1}\right) \\ \partial_t \mathbf{U}_i^1 &= \mathbf{L}_i^1\left(\mathbf{U}_{i-1}^{0,1}, \mathbf{U}_i^{0,1}, \mathbf{U}_{i+1}^{0,1}\right) \end{aligned} \tag{6}$$

in which, $\mathbf{L}_i^{0,1}$ are regarded as the discrete local representations of the conservation laws (1) for the average and the slope coefficients, respectively. They can be manipulated to give [15]

$$\mathbf{L}_i^0 = -\frac{\tilde{\mathbf{F}}_{i+1/2} - \tilde{\mathbf{F}}_{i-1/2}}{\Delta x} + \mathbf{S_b}\left(\mathbf{U}_i^0, z_i^1\right) \tag{7}$$

$$\begin{aligned} \mathbf{L}_i^1 = -\frac{3}{\Delta x}\Bigg\{ & \tilde{\mathbf{F}}_{i+1/2} + \tilde{\mathbf{F}}_{i-1/2} - \mathbf{F}\left(\mathbf{U}_i^0 + \frac{\hat{\mathbf{U}}_i^1}{\sqrt{3}}, z_i^0 + \frac{z_i^1}{\sqrt{3}}\right) - \mathbf{F}\left(\mathbf{U}_i^0 - \frac{\hat{\mathbf{U}}_i^1}{\sqrt{3}}, z_i^0 - \frac{z_i^1}{\sqrt{3}}\right) \\ & - \frac{\Delta x\sqrt{3}}{6}\left[\mathbf{S_b}\left(\mathbf{U}_i^0 + \frac{\hat{\mathbf{U}}_i^1}{\sqrt{3}}, z_i^1\right) - \mathbf{S_b}\left(\mathbf{U}_i^0 - \frac{\hat{\mathbf{U}}_i^1}{\sqrt{3}}, z_i^1\right)\right]\Bigg\} \end{aligned} \tag{8}$$

The fluxes, e.g. $\tilde{\mathbf{F}}_{i+1/2}$ across the interface $x_{i+1/2}$ (shared by the adjacent cells I_i and I_{i+1}), are obtained by solving the local Riemann problem defined by the two sets of states $\mathbf{U}_{i+1/2}^- \in I_i$ and $\mathbf{U}_{i+1/2}^+ \in I_{i+1}$

$$\begin{aligned} \mathbf{U}_{i+1/2}^- &= \mathbf{U_h}\left(x_{i+1/2}^-, t\right)\Big|_{I_i} = \mathbf{U}_i^0 + \hat{\mathbf{U}}_i^1 \\ \mathbf{U}_{i+1/2}^+ &= \mathbf{U_h}\left(x_{i+1/2}^+, t\right)\Big|_{I_{i+1}} = \mathbf{U}_{i+1}^0 - \hat{\mathbf{U}}_{i+1}^1 \end{aligned} \tag{9}$$

In (8) and (9), the slope coefficients with a "*hat*" symbol (e.g. $\hat{\mathbf{U}}_i^1$) have been slope-limited using approaches described later in Subsection 2.4. In the mean time, a "*depth-positivity-preserving*" version of the Riemann sates are reconstructed and then employed in the HLL flux formulae to evaluate the flux $\tilde{\mathbf{F}}_{i+1/2}$ as will be detailed in Subsection 2.3.

Finally, the approximate coefficients are advanced in time by a two-stage RK time integration scheme with a CFL = 0.3 for the time stepping constraint [15], i.e.

$$\left(\mathbf{U}_i^{0,1}\right)^{n+1/2} = \left(\mathbf{U}_i^{0,1}\right)^n + \Delta t\left(\mathbf{L}_i^{0,1}\right)^n \tag{10}$$

$$\left(\mathbf{U}_i^{0,1}\right)^{n+1} = \tfrac{1}{2}\left[\left(\mathbf{U}_i^{0,1}\right)^n + \left(\mathbf{U}_i^{0,1}\right)^{n+1/2} + \Delta t\left(\mathbf{L}_i^{0,1}\right)^{n+1/2}\right] \tag{11}$$

2.3 Wetting and drying condition

Similar to (9), the face values of water depth at either side of an interface $x_{i+1/2}$ (denoted by $h_{i+1/2}^{\pm}$) are evaluated by using the polynomial approximation to η_h-z_h, which is defined from free-surface elevation and topography data, i.e.

$$\begin{aligned} h_{i+1/2}^{-} &= \left(\eta_i^0 - z_i^0\right) + \widehat{\left(\eta_i^1 - z_i^1\right)} \\ h_{i+1/2}^{+} &= \left(\eta_{i+1}^0 - z_{i+1}^0\right) - \widehat{\left(\eta_{i+1}^1 - z_{i+1}^1\right)} \end{aligned} \tag{12}$$

which results in the slope-limited components of the water depth using the same slope-limiting approach as that for the flow variables (i.e. Section 2.4). Here, the depth slope component $\widehat{\left(\eta_i^1 - z_i^1\right)}$ represents the slope-limited output of the three input slope quantities $\eta_i^1 - z_i^1, \left(\eta_{i+1}^0 - z_{i+1}^0\right) - \left(\eta_i^0 - z_i^0\right)$ and $\left(\eta_i^0 - z_i^0\right) - \left(\eta_{i-1}^0 - z_{i-1}^0\right)$.

The associated velocities and topography approximations must be *numerically* evaluated from (9) and (12) for consistency (see the recent study of Mungkasi and Roberts [55]), i.e.

$$\begin{aligned} u_{i+1/2}^{\pm} &= q_{i+1/2}^{\pm} / h_{i+1/2}^{\pm} \\ z_{i+1/2}^{\pm} &= \eta_{i+1/2}^{\pm} - h_{i+1/2}^{\pm} \end{aligned} \tag{13}$$

In a dry cell I_i, in which the water depth is less than 10^{-8}, the face values of velocity are directly set to zero but not computed by (13). Obviously after (13), the continuity property of z_h may not hold anymore (since η_h and/or h_h can be discontinuous across $x_{i+1/2}$). It is necessary to define a single value of the bottom level at $x_{i+1/2}$ as

$$z_{i+1/2}^{*} = max(z_{i+1/2}^{-}, z_{i+1/2}^{+}) \tag{14}$$

Based on this single value of bed elevation, the *positivity-preserving* Riemann states of water depth can be defined as

$$h_{i+1/2}^{\pm,*} = max(0, \eta_{i+1/2}^{\pm} - z_{i+1/2}^{*}) \tag{15}$$

which are then used to reconstruct the associated *depth-positivity-preserving* Riemann states

$$\begin{aligned} \eta_{i+1/2}^{\pm,*} &= h_{i+1/2}^{\pm,*} + z_{i+1/2}^{*} \\ q_{i+1/2}^{\pm,*} &= h_{i+1/2}^{\pm,*} u_{i+1/2}^{\pm} \end{aligned} \tag{16}$$

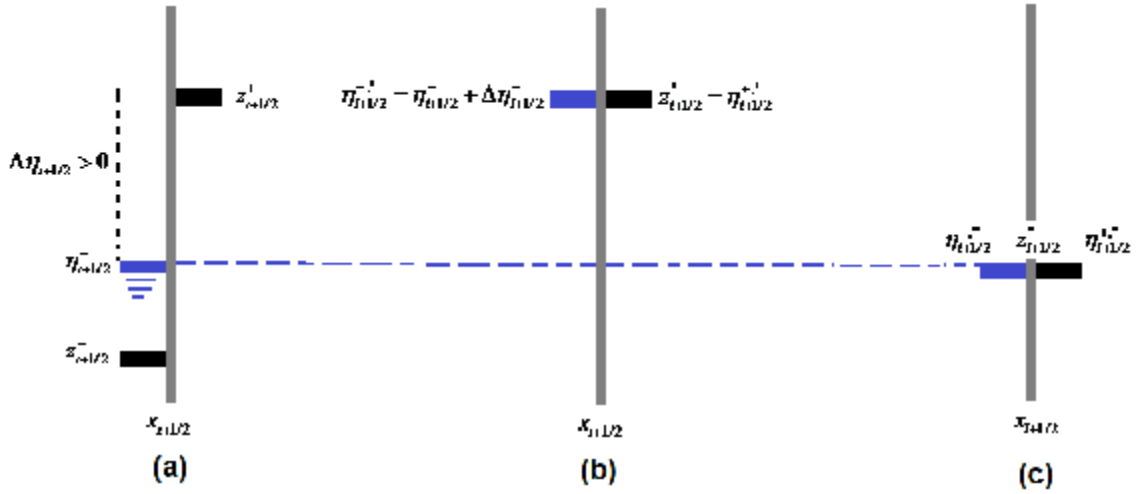

Fig 1: Second sub-case of a motionless wet/dry interface (i.e. $\eta_{i+1/2}^{-} < z_{i+1/2}^{*}$). **(a)** Initial free-surface states; **(b)** Forged free-surface states reconstructed by (13)-(16); **(c)** Local and temporal corrections (17)-(18) to bring back the original still free-surface state.

For a wet/wet interface at $x_{i+1/2}$ (i.e. $\eta_{i+1/2}^{\pm} > z_{i+1/2}^{*}$), the new Riemann states of the free-surface elevation obtained by (16) maintains its original level. The discharge components are defined according to the velocity components in (13) and therefore the initial momentum is conserved.

If $x_{i+1/2}$ is a dry/dry interface (i.e. $\eta_{i+1/2}^{\pm} = z_{i+1/2}^{\pm}$), (15) produces zero water depths and hence (16) defines a continuous free-surface elevation that is equal to the single bottom level given in (14). Apparently, the discharge components of Riemann states are both zero due to the zero water depths.

For a wet/dry interface $x_{i+1/2}$ (where a dry/wet interface can be treated similarly), two sub-cases must be considered, depending on the water level at the wet side. The first sub-case has a bed level at the dry side (right) that does not block the flow from the wet side (left), i.e. $\eta_{i+1/2}^{-} \geq z_{i+1/2}^{*}$ (it should be noted that this condition cannot hold stagnant water surface). This situation is correctly modelled by (13)-(16), which is essentially transferred into a standard Riemann problem onto a horizontal dry bed. For the second sub-case, the ground level at the dry side (right) is higher than the still water level at the wet side (left), i.e. $\eta_{i+1/2}^{-} < z_{i+1/2}^{*}$ (see Fig. 1a). Following (13)-(16), the initial Riemann state of free-surface elevation at the wet side ($\eta_{i+1/2}^{-}$) is overwritten to become, unrealistically, the same as the ground level defined at the dry side (i.e. $\eta_{i+1/2}^{-,*} = z_{i+1/2}^{*} \neq \eta_{i+1/2}^{-}$), which is actually equal to the free-surface elevation at the dry side (i.e. $\eta_{i+1/2}^{+,*} = z_{i+1/2}^{*}$; see Fig. 1b). This can trigger a fake momentum flux across the wet/dry interface and therefore affects the well-balanced property of the numerical scheme. To avoid this, the Riemann states of the free-surface elevation and the single value of bed topography are locally and temporally adjusted to be consistent with the initial wet free-surface level, ensuring continuous water surface at the concerned wet/dry interface (see Fig. 3c) [36], i.e.

$$\eta_{i+1/2}^{\pm,*} \leftarrow \eta_{i+1/2}^{\pm,*} - \Delta\eta_{i+1/2}^{-} \tag{17}$$

$$z_{i+1/2}^{*} \leftarrow z_{i+1/2}^{*} - \Delta\eta_{i+1/2}^{-} \tag{18}$$

where,

$$\Delta\eta_{i+1/2}^{-} = max\left[0, -\left(\eta_{i+1/2}^{-} - z_{i+1/2}^{*}\right)\right] \tag{19}$$

The Riemann states of discharge are correctly set to zero by (13)-(16) and therefore remain unchanged. By looking into Fig. 1 and Eq. (19), it is noted that $\Delta\eta_{i+1/2}^{-}$ is only positive in the case of a wet/dry interface with the wet side obstructed by the dry side (i.e. $\eta_{i+1/2}^{-} < z_{i+1/2}^{*}$).

Moreover, $\Delta\eta^{-}_{i+1/2}>0$ represents the erroneously increased level in the wet free-surface state (left) produced by (13)-(16). Therefore, (17)-(18) essentially bring back a continuous motionless state for the free-surface elevation and the single topography so that a balanced flux is produced by the HLL Riemann solver.

The *non-negative* Riemann states reconstructed after (13)–(16) and (17)–(19) are employed by the HLL solver to estimate the flux vector $\tilde{\mathbf{F}}_{i+1/2}$ across $x_{i+1/2}$. Denoting $\mathbf{U^L}=\left[\eta^{-,*}_{i+1/2};q^{-,*}_{i+1/2}\right]^{\mathrm{T}}$ and $\mathbf{U^R}=\left[\eta^{+,*}_{i+1/2};q^{+,*}_{i+1/2}\right]^{\mathrm{T}}$, together with $z^{*}_{i+1/2}$, the HLL flux $\tilde{\mathbf{F}}_{i+1/2}$ writes [48]

$$\tilde{\mathbf{F}}_{i+1/2}=\begin{cases}\mathbf{F^L} & \text{if } 0\le S^L\\ \mathbf{F^{LR}} & \text{if } S^L\le 0\le S^R\\ \mathbf{F^R} & \text{if } S^R\le 0\end{cases} \tag{20}$$

where, $\mathbf{F^L}=\mathbf{F(U^L)}$, $\mathbf{F^R}=\mathbf{F(U^R)}$ and $\mathbf{F^{LR}}$ contains the intermediate fluxes and is given by

$$\mathbf{F^{LR}}=\frac{S^R\mathbf{F^L}-S^L\mathbf{F^R}+S^LS^R\left(\mathbf{U^R}-\mathbf{U^L}\right)}{S^R-S^L} \tag{21}$$

The wave speeds S^L and S^R are calculated as [48]

$$S^L=\begin{cases}u^R-2\sqrt{gh^R} & \text{if } h^L\le 10^{-8}\\ \min\left(u^L-2\sqrt{gh^L},u^{LR}-2\sqrt{gh^{LR}}\right) & \text{otherwise}\end{cases} \tag{22}$$

$$S^R=\begin{cases}u^L+2\sqrt{gh^L} & \text{if } h^R\le 10^{-8}\\ \max\left(u^R+2\sqrt{gh^R},u^{LR}+2\sqrt{gh^{LR}}\right) & \text{otherwise}\end{cases} \tag{23}$$

where, $h^L=\eta^{-,*}_{i+1/2}-z^{*}_{i+1/2}$, $h^R=\eta^{+,*}_{i+1/2}-z^{*}_{i+1/2}$, $u^L=q^{-,*}_{i+1/2}/h^L$ (when $h^L>10^{-8}$; otherwise $u^L=0$) and $u^R=q^{+,*}_{i+1/2}/h^R$ (when $h^R>10^{-8}$; otherwise $u^R=0$). The intermediate states of depth and velocity components are found by

$$u^{LR}=\tfrac{1}{2}\left(u^R+u^L\right)-\left(\sqrt{gh^R}-\sqrt{gh^L}\right) \tag{24}$$

$$h^{LR} = \frac{1}{g}\left[\frac{1}{2}\left(\sqrt{gh^R} + \sqrt{gh^L}\right) - \frac{1}{4}\left(u^R - u^L\right)\right]^2 \tag{25}$$

In the frame of an RKDG2 scheme, values of the average and slope coefficients of the approximate solution and topography are also needed in order to evaluate the source terms for the local spatial operator $\mathbf{L}_i^0$ in (7) and the source and flux terms at the local Gaussian points for $\mathbf{L}_i^1$ in (8). In order to ensure a well-balanced scheme that preserves the non-negativity of water depth, the values of these local coefficients available at cell centres cannot be directly used but must be regenerated in compliance with the reconstructed positivity-preserving Riemann states and the associated topographic data. They may be obtained by recalculating the relationship (4) using the amended Riemann states and face values of topography

$$\bar{\mathbf{U}}_i^{0,1} = \frac{1}{2}\left(\mathbf{U}_{i+1/2}^{-,*} \pm \mathbf{U}_{i-1/2}^{+,*}\right) \tag{26}$$

$$\bar{z}_i^{0,1} = \frac{1}{2}\left(z_{i+1/2}^{-,*} \pm z_{i-1/2}^{+,*}\right) \tag{27}$$

As a whole, the fluxes $\tilde{\mathbf{F}}_{i+1/2}$ and $\tilde{\mathbf{F}}_{i-1/2}$ (estimated by a similar way as $\tilde{\mathbf{F}}_{i+1/2}$) as well as to the modified coefficients provided by (26)-(27) are used to evaluate the local spatial operators $\mathbf{L}_i^0$ and $\mathbf{L}_i^1$ and hence to update the flow variables in each cell during both stages of the RK flow updating procedure. It is worth noting that, at each RK stage, the original topography coefficients ($z_i^{0,1}$) stored at the cell centres are not changed and the adjustments in (27) are only locally and temporally generated for the evaluation of the spatial operators $\mathbf{L}_i^0$ and $\mathbf{L}_i^1$.

2.4 Local slope limiting

The controlled slope coefficients (i.e. those with the "*hat*" symbol) in (9) and (12) represent the output slope components provided by the FV *minmod* slope limiting approach, namely [15]

$$\hat{\mathbf{U}}_i^1 = minmod\left(\mathbf{U}_i^1, \mathbf{U}_{i+1}^0 - \mathbf{U}_i^0, \mathbf{U}_i^0 - \mathbf{U}_{i-1}^0\right) \tag{28}$$

The *minmod* function yields a zero slope if the signs of any two of the three input slopes are different. Otherwise, $\hat{\mathbf{U}}_i^1$ equals the slope with smallest magnitude. If it is uncontrollably performed as in an FV scheme (e.g. [34,49]) to limit the slope coefficient at all computational cells, (28) is referred to as a "Global Limiter" (GL). Although it is able to alleviate the numerical instability that may occur at the vicinity of the solution with steep gradients, a GL is reported to have a number of undesirable side effects as discussed in the Introduction.

Whenever possible, the limiting process should be localized to those necessary zones by adding a preliminary step to (28). The preliminary step collects those *troubled-slope-components* and specifies where slope-limited solution is necessary. The limiter thus becomes a "Local Limiter" (LL). Using an LL, (28) is only applied to those *troubled-slope-components* and the *untroubled-slope-components* are conserved, i.e. $\hat{\mathbf{U}}_i^1 = \mathbf{U}_i^1$. In this work, the *parameter-free* discontinuity-detection criterion of Krivodonova et al. [29] is implemented to localize the limiting process, i.e. (28) is locally active if the following condition is true

$$\mathbf{DS}_{i+1/2}^- > 1 \text{ or } \mathbf{DS}_{i-1/2}^+ > 1 \tag{29}$$

where $\mathbf{DS}_{i+1/2}^-$ and $\mathbf{DS}_{i-1/2}^+$ are the discontinuity detectors at the two cell edges ($x_{i+1/2}$ and $x_{i-1/2}$) within cell I_i. An explicit expression of $\mathbf{DS}_{i+1/2}^-$ is given by

$$\mathbf{DS}_{i+1/2}^- = \frac{\left|\mathbf{U}_{i+1/2}^+ - \mathbf{U}_{i+1/2}^-\right|}{\left|\frac{\Delta x}{2}\right| max\left(\left|\mathbf{U}_i^0 - \frac{\mathbf{U}_i^1}{\sqrt{3}}\right|, \left|\mathbf{U}_i^0 + \frac{\mathbf{U}_i^1}{\sqrt{3}}\right|\right)} \tag{30}$$

and $\mathbf{DS}_{i-1/2}^+$ may be similarly obtained.

As a result, the numerical solver associated with the LL is referred to as RKDG2-LL while the one implemented with the GL is called RKDG2-GL. Both of them will be tested and discussed further in Section 4.

Furthermore, it is reported that the slope limiting process (28) may become problematic if it is active in the vicinity of a wet/dry front (e.g. [10,17]). For instance, if cell I_i admits a wet/dry front at $x_{i+1/2}$ (i.e. cell I_{i+1} is dry), the slope-limiter may (unnecessarily) remove the actual local slope at cell I_i (defining the wet/dry front) and replace it by an irrelevant, or possibly an indefinite, slope quantity (e.g. for a dam-break wave propagating over an initially dry land). It is also important to note that the use of the localized limiting process, via (29), is not the best option to secure this problem as (30) may redundantly classify a local slope coefficient defining the wet/dry front as a damaged slope. Therefore, in the current wetting and drying algorithm, the principal slope ($\mathbf{U}_i^1$) is necessarily retained near a wet/dry front, i.e. $\hat{\mathbf{U}}_i^1 = \mathbf{U}_i^1$, if the cell under consideration is dry or adjacent to a dry cell. By noting that the solution to a wet/dry interface does not mathematically involve a shock wave formation [48], this measure not only removes the troublesome slope limiting process near a wet/dry front, but also maintains the second-order accuracy of the scheme (as will be seen later in Section 4).

2.5 Discretization of the friction source terms

To avoid the possible numerical instability induced by the inclusion of the friction terms [38], these terms should not be explicitly discretized in (7) and (8) but implicitly calculated using a splitting approach as in the FV schemes [11,12,35]. In an RKDG scheme, the local linear approximation to the friction terms may be denoted as $\left(\mathbf{S_f}\right)_h = \mathbf{S_f}\left(\eta_h, q_h, z_h\right)|_{I_i}$. The friction effect is then evaluated by implementing the following splitting implicit scheme

$$\frac{d\mathbf{U_h}}{dt} = \left(\mathbf{S_f}\right)_h^{n+1} \tag{31}$$

Since the friction increment is zero for the continuity equation, only the momentum component is actually considered, i.e.

$$\frac{dq_h}{dt} = \left(S_f\right)_h^{n+1} \tag{32}$$

This may be approximated by

$$\frac{q_h^{n+1} - q_h^n}{\Delta t} = \left(S_f\right)^{n+1} = \left(S_f\right)^n + \frac{\partial \left(S_f\right)_h^n}{\partial q}\left(q_h^{n+1} - q_h^n\right) \tag{33}$$

which produces the following time stepping formula for q_h

$$q_h^{n+1} = q_h^n + \Delta t \frac{\left(S_f\right)_h^n}{D_h^n} \tag{34}$$

and D_h^n is the implicit coefficient given by

$$D_h^n = 1 + 2\Delta t \left(C_f\right)_h^n \left|u_h^n\right| / h_h^n \tag{35}$$

This implicit discretization of friction source term automatically ensures $q_h^n \times q_h^{n+1} \geq 0$ and will not predict a reversed flow. In the current RKDG2 scheme, the above splitting implicit scheme (34) is applied to each wet cell to compute the averaged coefficients (q_i^0) in a pointwise manner. In order to add the friction contribution to the slope coefficients (q_i^1), one simple way is to perform two pointwise friction updates at the intermediate Gaussian points ($q_{\mathbf{G1}}^{n+1}$ and $q_{\mathbf{G2}}^{n+1}$) and then deduce the slope coefficients by the following P^1-projection approximate relationship [15,28]

$$\left(q_i^1\right)^{n+1} = \tfrac{\sqrt{3}}{2}\left(q_{\mathbf{G1}}^{n+1} - q_{\mathbf{G2}}^{n+1}\right) \tag{36}$$

In (36), $q_{\mathbf{G1}}^{n+1}$ and $q_{\mathbf{G2}}^{n+1}$ represent the two friction updates $q_{\mathbf{G1,G2}}^n = \left(q_i^0 \pm q_i^1 / \sqrt{3}\right)^n$, which are obtained by following (34).

The above friction calculations are only necessary in those wet cells as no friction exists due to zero flow in a dry cell. At the beginning of each RK stage, the implicit friction

discretization is performed and the resulting flow updates are used as the initial values for the operators in (7) and (8).

3. Main properties of the current RKDG2 scheme

Theorem 3.1: The RKDG2 scheme, with the Riemann states reconstructed by following (13)-(19) and their associated local adjustments obtained from (26)-(27) for the flow variables and the topography coefficients, is well-balanced for the still water stationary state.

Proof: For a general problem of lake at rest defined by $\eta = constant$ at the wet areas and $q = 0$, after removing the terms with zero velocity in the shallow water equations (1)-(2), only the following part of the momentum equation mathematically remains

$$\frac{g}{2}\left(\eta^2 - 2\eta z\right)_x = -g\eta z_x \tag{37}$$

The momentum flux, which will be evaluated by the HLL Riemann solver, becomes

$$f = \frac{g}{2}\left(\eta^2 - 2\eta z\right)_x \tag{38}$$

For the $\mathbf{L}_i^0$ operator, the bed slope source term is numerically approximated as

$$S_b\left(\overline{\eta}_i^0, \overline{z}_i^1\right) = -g\overline{\eta}_i^0 \frac{2\overline{z}_i^1}{\Delta x} \tag{39}$$

For the $\mathbf{L}_i^1$ operator, the local intermediate fluxes must also be calculated

$$f\left(\overline{\eta}_i^0 \pm \frac{\overline{\eta}_i^1}{\sqrt{3}}, \overline{z}_i^0 \pm \frac{\overline{z}_i^1}{\sqrt{3}}\right) = \frac{g}{2}\left[\left(\overline{\eta}_i^0 \pm \frac{\overline{\eta}_i^1}{\sqrt{3}}\right)^2 - 2\left(\overline{\eta}_i^0 \pm \frac{\overline{\eta}_i^1}{\sqrt{3}}\right)\left(\overline{z}_i^0 \pm \frac{\overline{z}_i^1}{\sqrt{3}}\right)\right] \tag{40}$$

and the corresponding contribution of the source term is

$$S_b\left(\overline{\eta}_i^0 \pm \frac{\overline{\eta}_i^1}{\sqrt{3}}, \overline{z}_i^1\right) = -g\left(\overline{\eta}_i^0 \pm \frac{\overline{\eta}_i^1}{\sqrt{3}}\right)\frac{2\overline{z}_i^1}{\Delta x} \tag{41}$$

Herein $\overline{\eta}_i^{0,1}$ and $\overline{z}_i^{0,1}$ are the local linear approximations to the free-surface elevation (η_h) and the topography (z_h) produced by (26) and (27).

We first prove that the solution to a still steady flow over irregular topography is numerically retained for a cell (I_i) with wet/wet interfaces at both $x_{i-1/2}$ and $x_{i+1/2}$ (*i.e.* cells I_{i-1}, I_i and I_{i+1} are all wet). In this case, the wetting and drying reconstruction following (13)-(16) conserves the original free-surface elevation at both interfaces (*i.e.* $\eta_{i\pm1/2}^{-,*}=\eta_{i\pm1/2}^{-}$ and $\eta_{i\pm1/2}^{+,*}=\eta_{i\pm1/2}^{+}$) and (26) thus retrieves the local initial free-surface elevation (*i.e.* $\overline{\eta}_i^0=\eta_i^0$ and $\overline{\eta}_i^1=\eta_i^1$) defined by (4). Moreover, the free-surface elevation is continuous across $x_{i-1/2}$ and $x_{i+1/2}$ (*i.e.* $\eta_{i\pm1/2}^{-}=\eta_{i\pm1/2}^{+}$), owing to the constant (wet) free-surface level. The lake at rest hypothesis holds at the approximate level and η_h is locally constant, *i.e.* $\overline{\eta}_i^0=\eta$ and $\overline{\eta}_i^1=0$. Therefore (26)-(27) yields $\overline{\eta}_i^0=\eta_{i+1/2}^{-,*}=\eta_{i-1/2}^{+,*}=\eta$. Consequently, $\overline{\eta}_i^0=\eta_{i+1/2}^{\pm,*}=\eta_{i-1/2}^{\pm,*}=\eta$ and (38) and (39) write $f_{i\pm1/2}=\frac{g}{2}\left[\eta^2-2\eta z_{i\pm1/2}^{*}\right]$ and $S_b\left(\overline{\eta}_i^0,\overline{z}_i^1\right)=-g\eta\frac{2\overline{z}_i^1}{\Delta x}$. The momentum entry for $\mathbf{L}_i^0$ in (7) is then balanced to zero, i.e.

$$\begin{aligned}\left(L_i^0\right)^{mom}&=-\tfrac{1}{\Delta x}\left[f_{i+1/2}-f_{i-1/2}\right]+S_b\left(\overline{\eta}_i^0,\overline{z}_i^1\right)\\&=-\tfrac{1}{\Delta x}\left[\tfrac{g}{2}(-2\eta)\left(z_{i+1/2}^{*}-z_{i-1/2}^{*}\right)\right]+\left(-g\eta\tfrac{2\overline{z}_i^1}{\Delta x}\right)\\&=\ 0\end{aligned}\qquad(42)$$

Eqs. (40) and (41) condenses to $f\left(\overline{\eta}_i^0\pm\frac{\overline{\eta}_i^1}{\sqrt{3}},\overline{z}_i^0\pm\frac{\overline{z}_i^1}{\sqrt{3}}\right)=\frac{g}{2}\left[\eta^2-2\eta\left(\overline{z}_i^0\pm\frac{\overline{z}_i^1}{\sqrt{3}}\right)\right]$ and $S_b\left(\overline{\eta}_i^0\pm\frac{\overline{\eta}_i^1}{\sqrt{3}},\overline{z}_i^1\right)=-g\eta\frac{2\overline{z}_i^1}{\Delta x}$, respectively, which compute zero momentum component for the $\mathbf{L}_i^1$ operator in (8), i.e.

$$
\begin{aligned}
\left(L_i^1\right)^{mom} &= -\tfrac{3}{\Delta x}\Big\{f_{i+1/2}+f_{i-1/2}-f\left(\overline{\eta}_i^0+\tfrac{\overline{\eta}_i^1}{\sqrt{3}},\overline{z}_i^0+\tfrac{\overline{z}_i^1}{\sqrt{3}}\right)-f\left(\overline{\eta}_i^0-\tfrac{\overline{\eta}_i^1}{\sqrt{3}},\overline{z}_i^0-\tfrac{\overline{z}_i^1}{\sqrt{3}}\right)\\
&\qquad -\tfrac{\Delta x\sqrt{3}}{6}\left[S_b\left(\overline{\eta}_i^0+\tfrac{\overline{\eta}_i^1}{\sqrt{3}},\overline{z}_i^1\right)-S_b\left(\overline{\eta}_i^0-\tfrac{\overline{\eta}_i^1}{\sqrt{3}},\overline{z}_i^1\right)\right]\Big\}\\
&= -\tfrac{3}{\Delta x}\Big\{\tfrac{g}{2}\left[2\eta^2-2\eta\left(z_{i+1/2}^*+z_{i-1/2}^*\right)\right]-\tfrac{g}{2}\left[\eta^2-2\eta\left(\overline{z}_i^0+\tfrac{\overline{z}_i^1}{\sqrt{3}}\right)\right]-\tfrac{g}{2}\left[\eta^2-2\eta\left(\overline{z}_i^0-\tfrac{\overline{z}_i^1}{\sqrt{3}}\right)\right]\\
&\quad -\tfrac{\Delta x\sqrt{3}}{6}\left[\left(-g\eta\tfrac{2\overline{z}_i^1}{\Delta x}\right)-\left(-g\eta\tfrac{2\overline{z}_i^1}{\Delta x}\right)\right]\Big\}=-\tfrac{3}{\Delta x}\Big\{\tfrac{g}{2}\left[2\eta^2-4\eta\overline{z}_i^0\right]-\tfrac{g}{2}\left[2\eta^2-4\eta\overline{z}_i^0\right]\Big\}=0
\end{aligned}
\tag{43}
$$

Obviously, the initial quiescent conditions stay unchanged within each RK time stage for the wet-bed cases. Hence, the well-balanced solutions are ensured in the wet parts of the domain.

For a wet cell I_i with a partially wet interface, without loss of generality, we assume that $x_{i-1/2}$ is wet (wet/wet) while $x_{i+1/2}$ is wet/dry (i.e. cells I_{i-1} and I_i are wet but cell I_{i+1} is dry). At $x_{i-1/2}$, the present reconstruction process yields $\eta_{i-1/2}^{-,*}=\eta_{i-1/2}^{+,*}=\eta$. At $x_{i+1/2}$, lake at rest problem can only exist in the case with the dry ground higher than or equal to the actual water level at I_i (i.e. $\eta_{i+1/2}^{-}\le z_{i+1/2}^{+}$). After implementing the non-negative reconstruction of Riemann states in (13)-(16) and obtaining $\eta_{i+1/2}^{\pm,*}=z_{i+1/2}^*$, (17)-(19) are then active to ensure that $\eta_{i+1/2}^{\pm,*}=z_{i+1/2}^*=\eta$. This case is now similar to the aforementioned fully wet case and therefore the well-balanced solution is guaranteed.

For a dry cell I_i, with dry/dry interfaces at both $x_{i-1/2}$ and $x_{i+1/2}$ (i.e. cells I_{i-1}, I_i and I_{i+1} are all dry), $\eta_{i-1/2}^{\pm,*}=z_{i-1/2}^*$ and $\eta_{i+1/2}^{\pm,*}=z_{i+1/2}^*$, the fluxes from (38) and the source term in (39) reduce, respectively, to $f_{i\pm1/2}=-\tfrac{g}{2}\left(z_{i\pm1/2}^*\right)^2$ and $S_b\left(\overline{\eta}_i^0,\overline{z}_i^1\right)=-g\overline{z}_i^0\tfrac{2\overline{z}_i^1}{\Delta x}$, which result in zero momentum entry in (7) as follows

$$
\begin{aligned}
\left(L_i^0\right)^{mom} &= -\tfrac{1}{\Delta x}\left[f_{i+1/2}-f_{i-1/2}\right]+S_b\left(\overline{\eta}_i^0,\overline{z}_i^1\right)\\
&= -\tfrac{1}{\Delta x}\left[-\tfrac{g}{2}\left(z_{i+1/2}^*\right)^2-\left(z_{i-1/2}^*\right)^2\right]-g\overline{z}_i^0\tfrac{2\overline{z}_i^1}{\Delta x}\\
&= -\tfrac{1}{\Delta x}\left[-\tfrac{g}{2}\left(z_{i+1/2}^*+z_{i-1/2}^*\right)\left(z_{i+1/2}^*-z_{i-1/2}^*\right)\right]-g\left(\tfrac{z_{i+1/2}^*+z_{i-1/2}^*}{2}\right)\tfrac{\left(z_{i+1/2}^*-z_{i-1/2}^*\right)}{\Delta x}\\
&= 0
\end{aligned}
\tag{44}
$$

The fluxes (40) and source terms (41) become $f\left(\overline{\eta}_i^0 \pm \frac{\overline{\eta}_i^1}{\sqrt{3}}, \overline{z}_i^0 \pm \frac{\overline{z}_i^1}{\sqrt{3}}\right) = -\frac{g}{2}\left(\overline{z}_i^0 \pm \frac{\overline{z}_i^1}{\sqrt{3}}\right)^2$ and $S_b\left(\overline{\eta}_i^0 \pm \frac{\overline{\eta}_i^1}{\sqrt{3}}, \overline{z}_i^1\right) = -g\left(\overline{z}_i^0 \pm \frac{\overline{z}_i^1}{\sqrt{3}}\right)\frac{2\overline{z}_i^1}{\Delta x}$, which also lead to zero operator of (8), i.e.

$$
\begin{aligned}
\left(L_i^1\right)^{mom} &= -\frac{3}{\Delta x}\left\{f_{i+1/2} + f_{i-1/2} - f\left(\overline{\eta}_i^0 + \frac{\overline{\eta}_i^1}{\sqrt{3}}, \overline{z}_i^0 + \frac{\overline{z}_i^1}{\sqrt{3}}\right) - f\left(\overline{\eta}_i^0 - \frac{\overline{\eta}_i^1}{\sqrt{3}}, \overline{z}_i^0 - \frac{\overline{z}_i^1}{\sqrt{3}}\right)\right. \\
&\qquad \left. - \frac{\Delta x\sqrt{3}}{6}\left[S_b\left(\overline{\eta}_i^0 + \frac{\overline{\eta}_i^1}{\sqrt{3}}, \overline{z}_i^1\right) - S_b\left(\overline{\eta}_i^0 - \frac{\overline{\eta}_i^1}{\sqrt{3}}, \overline{z}_i^1\right)\right]\right\} \\
&= -\frac{3}{\Delta x}\left\{-\frac{g}{2}\left[\left(z_{i+1/2}^*\right)^2 + \left(z_{i-1/2}^*\right)^2\right] + g\left[\left(\overline{z}_i^0\right)^2 + \frac{1}{3}\left(\overline{z}_i^1\right)^2\right] + \frac{2g}{3}\left(\overline{z}_i^1\right)^2\right\} \\
&= -\frac{3}{\Delta x}\left\{-\frac{g}{2}\left[\left(z_{i+1/2}^*\right)^2 + \left(z_{i-1/2}^*\right)^2\right] + g\left[\left(\overline{z}_i^0\right)^2 + \left(\overline{z}_i^1\right)^2\right]\right\} \\
&= -\frac{3}{\Delta x}\left\{-\frac{g}{2}\left[\left(z_{i+1/2}^*\right)^2 + \left(z_{i-1/2}^*\right)^2\right] + g\left[\left(\frac{z_{i+1/2}^* + z_{i-1/2}^*}{2}\right)^2 + \left(\frac{z_{i+1/2}^* - z_{i-1/2}^*}{2}\right)^2\right]\right\} \\
&= -\frac{3}{\Delta x}\left\{-\frac{g}{2}\left[\left(z_{i+1/2}^*\right)^2 + \left(z_{i-1/2}^*\right)^2\right] + \frac{g}{2}\left[\left(z_{i+1/2}^*\right)^2 + \left(z_{i-1/2}^*\right)^2\right]\right\} = 0
\end{aligned}
\tag{45}
$$

Hence, the well-balanced solutions are ensured in the dry zones.

For a dry cell I_i with a partially wet interface; for instance, a wet/dry interface $x_{i-1/2}$ and a dry/dry interface $x_{i+1/2}$. At $x_{i+1/2}$ (13)-(16) reconstruct $\eta_{i+1/2}^{\pm,*} = z_{i+1/2}^*$.At the dry side of $x_{i-1/2}$, which should be obstructing the flow from the other side, we should at least have $\eta_{i-1/2}^{+,*} = z_{i-1/2}^*$. This case can be treated similarly to the fully dry case investigated previously and therefore the well-balanced solution is guaranteed at a dry cell that admits a dry/wet interface (i.e. adjacent to a motionless wet cell).

Theorem 3.2: The RKDG2 scheme, with the Riemann states reconstructed by following (13)-(19) and their associated local adjustments obtained from (26)-(27) for the flow variables and topography coefficients, conserves the positivity of the time-evolving average water depth.

Proof: From (13)-(15), the following inequality can be easily derived

$$0 \le h_{i\pm1/2}^{\pm,*} \le h_{i\pm1/2}^{\pm} \tag{46}$$

The local average and slope coefficients of water depth, used in the space discretization operators (7) and (8), can be calculated using (26) and (27) together with (16) as:

$$\begin{aligned} \overline{\eta}_i^0 - \overline{z}_i^0 &= \tfrac{1}{2}\left(h_{i+1/2}^{-,*} + h_{i-1/2}^{+,*}\right) \\ \overline{\eta}_i^1 - \overline{z}_i^1 &= \tfrac{1}{2}\left(h_{i+1/2}^{-,*} - h_{i-1/2}^{+,*}\right) \end{aligned} \tag{47}$$

It is evident from (46) and (47) that the reconstructed local average coefficient of the water height is always non-negative (i.e. $\overline{\eta}_i^0 - \overline{z}_i^0 \geq 0$). When calculating the space discretization operator $\mathbf{L}_i^1$ in (8), the water depth at the intermediate Gaussian points must also be available, which can be expressed as a linear combination of $h_{i-1/2}^{+,*}$, $h_{i+1/2}^{-,*}$ with positive weights $1 \mp \frac{\sqrt{3}}{3} > 0$, i.e.

$$\left(\overline{\eta}_i^0 - \overline{z}_i^0\right) \pm \tfrac{\sqrt{3}}{3}\left(\overline{\eta}_i^1 - \overline{z}_i^1\right) = \tfrac{1}{2}\left[\left(1 \pm \tfrac{\sqrt{3}}{3}\right)h_{i+1/2}^{-,*} + \left(1 \mp \tfrac{\sqrt{3}}{3}\right)h_{i-1/2}^{+,*}\right] \tag{48}$$

Therefore, although the slope coefficient $\overline{\eta}_i^1 - \overline{z}_i^1$ does not own the non-negative property, the water depth at the intermediate Gaussian points is *positivity-preserving*. From (46), (47), (13) and (4) it can be also demonstrated that

$$0 \leq \overline{\eta}_i^0 - \overline{z}_i^0 \leq \left(\eta_i^0\right)^n - z_i^0 \tag{49}$$

where $\left(\eta_i^0\right)^n - z_i^0$ is the water depth at the cell centre of cell I_i at $t = n$.

Based on the above conditions, we can now prove that the present wetting and drying approach ensures non-negativity of water depth (i.e. the average coefficient of water depth) at an arbitrary cell I_i. In practical simulations, there are two types of wet/dry fronts, i.e. advancing wet/dry fronts (assuming $u \geq 0$) and retreating wet/dry fronts (assuming $u \leq 0$). We only investigate the advancing wet/dry fronts but the retreating wet/dry fronts can be investigated by following a similar procedure. An advancing wet/dry front with $u \geq 0$ may be generalized into the following two classes:

(a) Cell I_i has a wet/wet interface on the left at $x_{i-1/2}$ and a wet/dry one on the right at $x_{i+1/2}$, i.e. cells I_{i-1}, I_i are wet while cell I_{i+1} is dry;

(b) Cell I_i has a wet/dry interface on the left at $x_{i-1/2}$ and a dry/dry one on its right at $x_{i+1/2}$, i.e. cells I_{i-1} is wet while cells I_i and I_{i+1} are dry.

There are actually two sub-cases in class (a), depending on whether the ground level at the dry cell I_{i+1} is higher than the actual water level at I_i or not. If the flow is blocked by the dry cell, i.e. the dry bed level is higher than the incoming water level, the discharge leaving the cell under consideration (I_i) is calculated to be zero by the aforementioned wetting and drying technique. Therefore, the water depth at cell I_i will be always predicted to be positive. However, the case with the ground level at cell I_{i+1} lower than the water level at I_i is not as trivial and will be investigated in more details in this section. In this case, the worst scenario occurs when cell I_i does not receive mass from cell I_{i-1} but loose water to cell I_{i+1}. We have to prove that the mean water height at cell I_i at $t = n+1$ is non-negative, i.e. $\left(\eta_i^0\right)^{n+1} - z_i^0 \geq 0$, provided that $\left(\eta_i^0\right)^n - z_i^0 \geq 0$ at $t = n$.

Without losing generality, we consider the discrete update of the mass equation using an explicit Euler-forward time stepping, which may be regarded as one of the updating steps of the two-stage RK method in (10). The average coefficient of the free-surface elevation is forwarded to the next time level as

$$\left(\eta_i^0\right)^{n+1} = \left(\eta_i^0\right)^n - \frac{\Delta t}{\Delta x}\left[\tilde{f}_{i+1/2}^{mass} - \tilde{f}_{i-1/2}^{mass}\right] \tag{50}$$

where $\tilde{f}_{i\pm1/2}^{mass}$ are the HLL fluxes computed after applying the wetting and drying algorithm (13)-(19). As previously mentioned, we assume $\tilde{f}_{i-1/2}^{mass} = 0$ and the flux between cell I_i and cell I_{i+1} is determined by the HLL Riemann solver as $\tilde{f}_{i+1/2}^{mass} = h_{i+1/2}^{-,*} u$. Therefore, after subtracting z_i^0 from both sides, (50) may be rewritten as

$$\left[\left(\eta_i^0\right)^{n+1}-z_i^0\right]=\left[\left(\eta_i^0\right)^{n}-z_i^0\right]-\tfrac{\Delta t}{\Delta x}h_{i+1/2}^{-,*}u \tag{51}$$

From (47) and (49), the following inequality can be also obtained

$$h_{i+1/2}^{-,*}\le 2\left(\overline{\eta}_i^0-\overline{z}_i^0\right)\le 2\left[\left(\eta_i^0\right)^{n}-z_i^0\right] \tag{52}$$

Combining (51) and (52), we have

$$\left[\left(\eta_i^0\right)^{n+1}-z_i^0\right]\ge\left(1-2\,\mathrm{CFL}\right)\left[\left(\eta_i^0\right)^{n}-z_i^0\right] \tag{53}$$

where $\mathrm{CFL}=u\frac{\Delta t}{\Delta x}$ denotes the CFL number, which is defined based on the fact that the water depth is vanishing near the wet/dry front and so the wave speed is near zero. From (53), it is evident that the water depth at the new time step is non-negative if the CFL number is chosen to be no greater than 0.5. The condition is satisfied as CFL = 0.3 is used in this work as mentioned in Section 2.2.

For the case (b), *non-negativity of water depth* is more trivial to prove as no calculation is involved between cell I_i and I_{i+1} while I_i is receiving mass from cell I_{i-1}, i.e.

$$\left[\left(\eta_i^0\right)^{n+1}-z_i^0\right]=\left[\left(\eta_i^0\right)^{n}-z_i^0\right]+\tfrac{\Delta t}{\Delta x}h_{i-1/2}^{+,*}u \tag{54}$$

Since $\left(\eta_i^0\right)^{n}-z_i^0\ge 0$ and the $\frac{\Delta t}{\Delta x}h_{i-1/2}^{+,*}u$ is also positive, it can be clearly concluded that $\left(\eta_i^0\right)^{n+1}-z_i^0\ge 0$.

4. Numerical results and discussions

This section validates the present RKDG2 algorithm and meanwhile assesses the importance of the local slope limiting in practical flow simulations. For these purposes, the numerical codes are used to simulate several challenging wet or dry-bed test cases involving steady and unsteady shallow flows over continuous/discontinuous topographies with/without friction.

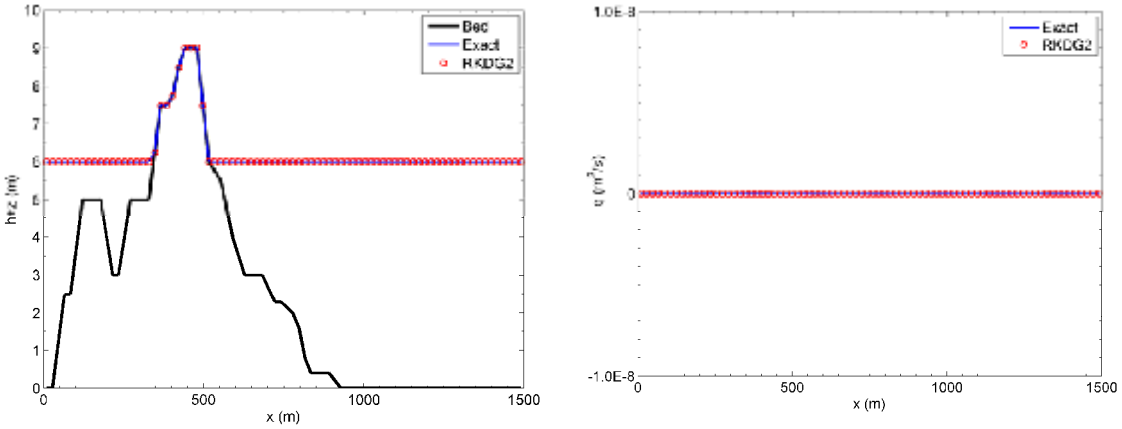

Fig. 2: Quiescent flow: RKDG2 predicted flow profiles at t = 5000s.

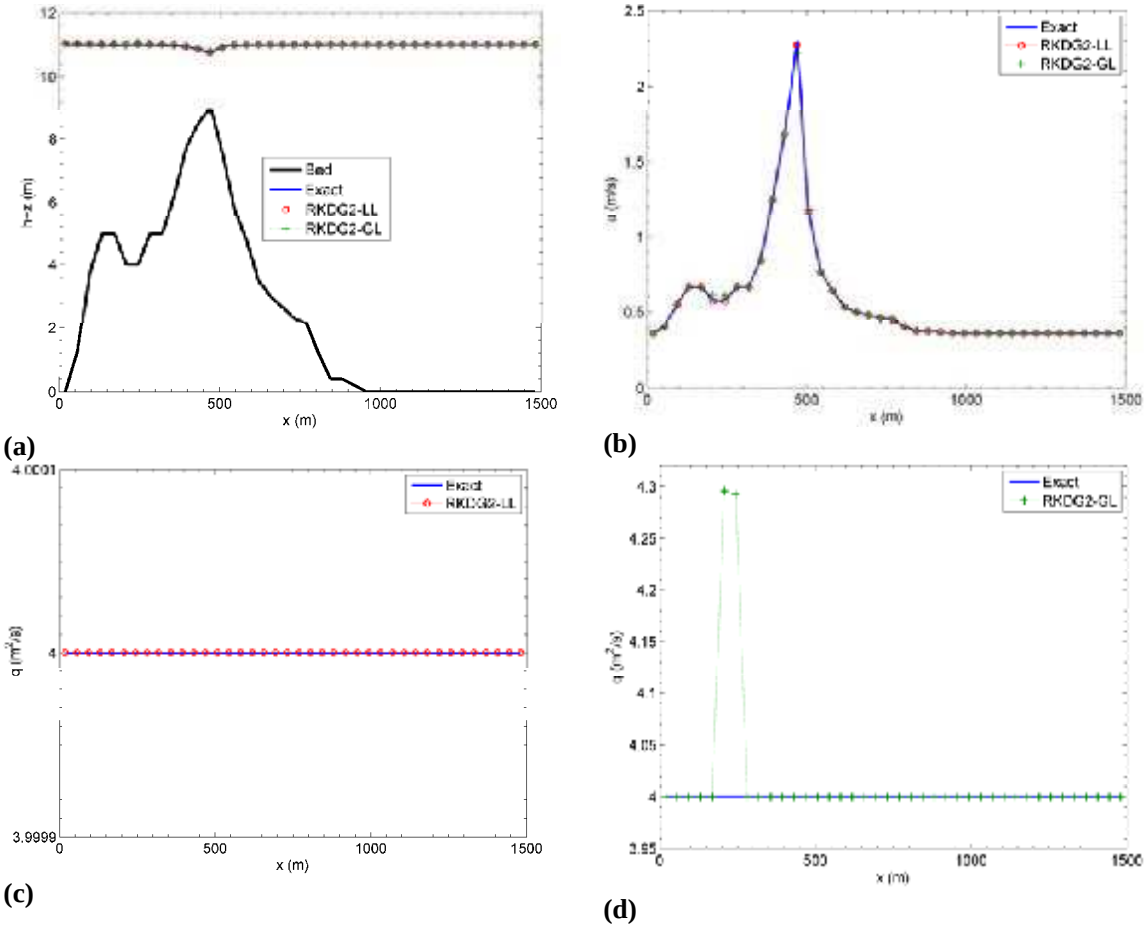

Fig. 3: Smooth steady flow over irregular topography; flow profiles at t = 5000s: **(a)** free-surface elevation, **(b)** velocities; **(c)** RKDG2-LL discharge and **(d)** RKDG2-GL discharge.

4.1. Quiescent flow test with wet/dry fronts

We consider a quiescent flow test case in a 1500m long frictionless domain with an irregular topographic profile that contains non-differentiable points [28]. The domain is first assumed

to be partially submerged and closed by solid walls. The initial conditions are $\eta(x,0) = max[6, z(x)]$ and $q(x,0) = 0$, which should be numerically maintained by a well-balanced numerical scheme. A uniform grid with 80 cells is used for the simulations and reflective boundary conditions are imposed. The RKDG2-LL predictions at t = 5000s are presented in Fig. 2, where the free-surface elevation remains unperturbed throughout the simulation and the zero discharge is accurately reproduced. Although it is not displayed, the current numerical scheme also guarantees mass conservation and the mass error also remains in the range of round-off error. In this test the RKDG2-LL and RKDG2-GL give nearly identical results.

The test case is slightly modified so that the domain is submerged and a smooth steady flow is assumed to have a water level of 11m and a discharge of $4m^2/s$. To allow a quantitative comparison between the RKDG2-GL and the RKDG2-LL codes, simulations are run with N = 40 cells until t = 5000s when steady-state solutions are obtained. Transmissive boundary conditions are imposed with fixed inflow discharge and outflow depth. The RKDG2-GL and the RKDG2-LL calculations are illustrated in Fig. 3, compared with the exact solutions. Both the RKDG2-GL and RKDG2-LL predictions are observed to follow closely the analytical water level (i.e. Fig. 3a) and the velocity (i.e. Fig. 3b)—where the RKDG2-LL traces more accurately the local flow zone over the steepest gradients. For the discharge only RKDG2-LL gives satisfactory result (i.e. Fig. 3c) and the RKDG2-GL output is apparently divergent from the analytical solution at certain locations (see Fig. 3d—also notice the difference between the q-axis scales). However, although it is not illustrated here, it is important to note that the RKDG2-GL calculation of discharge tends to significantly improve with increasing grid refinement (e.g. $N \geq 80$). While proving the capability of the current RKDG2 scheme in handling general steady flow problems, the test also provides an insight on the inability of a global limiter in conserving momentum.

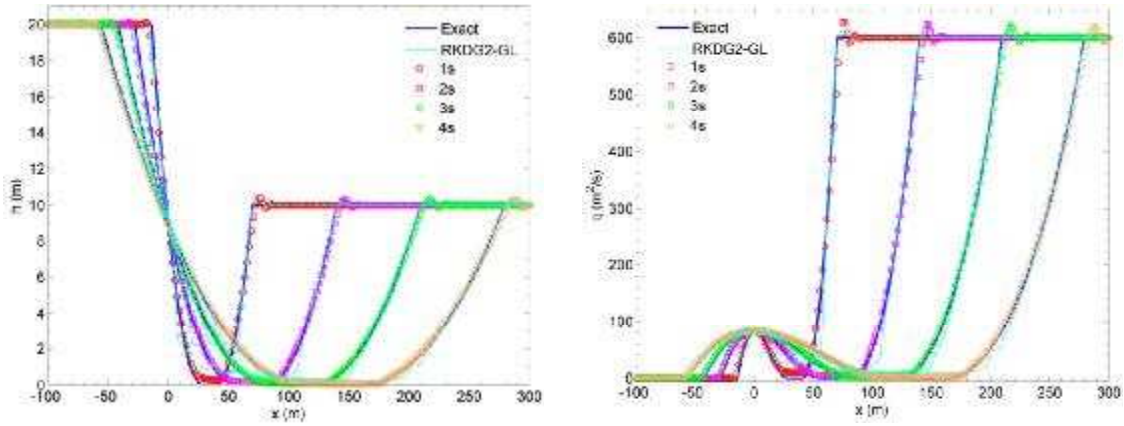

Fig. 4: RKDG2 solutions to the Riemann problem at different output times (N = 320). Sub-case 1: vacuum-type flow.

4.2. Riemann problems over a frictionless flat bed

As in [10], two-type of Riemann problems involving wetting and drying are considered to demonstrate the capability of the current RKDG2 codes in maintaining non-negative water depth. The first sub-case involves a vacuum-type flow in a 600m long domain defined as [-200m; 400m]. The initial conditions are provided as in [48]

$$h(x,0)=\begin{cases}20 & \text{if } x\le 0\\ 10 & \text{otherwise}\end{cases} \text{ and } u(x,0)=\begin{cases}0 & \text{if } x\le 0\\ 60 & \text{otherwise}\end{cases} \tag{55}$$

After it is released at t = 0s, the initial flow develops into two depression waves and produces a dry area, or vacuum, in between, which is numerically difficult to reproduce. All of the boundary conditions are set to be transmissive. Simulations are carried out on different computational grids with N = 20, 40, 80, 160 and 320 cells, respectively, up to t = 4s. The snapshots of flow profiles are presented in Fig. 4 (for N = 320) for t = 1, 2, 3 and 4s in the reach [-100m; 300m] of the computational domain. The RKDG2-LL predictions (plotted using markers) are observed to accurately follow the evolution of the wet/dry process and the two depression waves suggested by the analytical solutions. Table 1 and Table 2 list the errors and order of convergence evaluated at t = 1s and t = 4s, which confirms the overall second-order accuracy of the predictions. Despite the overall accurate predictions obtained by RKDG2-LL, apparent numerical oscillations are also detected around the downstream

propagating discontinuous kink. Fortunately, these less accurate predictions are essentially local and do not propagate with time. Furthermore, their existence is not actually related to the proposed wetting and drying algorithm, but links to the fact that Krivodonova et al. [29] detector sometimes tends to overlook a weak discontinuity. In contrast, the upstream propagating discontinuity kink is much better handled. Also in Fig. 4, the RKDG2-GL calculations are plotted using a thin dashed line to reveal the much less accurate results produced by the GL when modelling this vacuum-type flow.

Table 1a: L^1–Error and order of accuracy at t = 1s. Sub-case 1: vacuum-type flow.

No. of cells (N)				
	$h + z$ (m)		q (m^2/s)	
	L^1–Errors	L^1–Rate	L^1–Errors	L^1–Rate
20	3.9106E-003	--	4.2281E-003	--
40	8.4408E-004	2.212	9.9476E-004	2.087
80	2.8752E-004	1.553	2.6866E-004	1.888
160	5.0896E-005	2.498	5.6545E-005	2.248
320	1.7604E-005	1.5316	1.6520E-005	1.775

Table 1b: L^∞–Error and order of accuracy at t = 1s. Sub-case 1: vacuum-type flow.

No. of cells (N)				
	$h + z$ (m)		q (m^2/s)	
	L^∞–Errors	L^∞–Rate	L^∞–Errors	L^∞–Rate
20	2.5319E-002	--	1.7463E-002	--
40	5.1808E-003	2.289	7.6968E-003	1.182
80	3.2781E-003	0.660	1.6315E-003	2.238
160	6.8847E-004	2.251	9.8002E-004	0.735
320	2.8285E-004	1.283	2.3324E-004	2.071

Table 2a: L^1–Error and order of accuracy at t = 4s. Sub-case 1: vacuum-type flow.

No. of cells (N)				
	$h + z$ (m)		q (m^2/s)	
	L^1–Errors	L^1–Rate	L^1–Errors	L^1–Rate
20	5.9992E-003	--	9.2080E-003	--
40	1.1034E-003	2.442	1.9128E-003	2.2672
80	3.8948E-004	1.502	5.6008E-004	1.7720
160	7.0103E-005	2.474	1.2164E-004	2.2030
320	2.3644E-005	1.568	3.4844E-005	1.8037

Table 2b: L^∞–Errors and order of accuracy at t = 4s. Sub-case 1: vacuum-type flow.

No. of cells (N)				

	$h+z$ (m)		q (m^2/s)	
	L^∞–Errors	L^∞–Rate	L^∞–Errors	L^∞–Rate
20	1.3397E-002	--	9.2080E-002	--
40	2.8979E-003	2.208	3.9090E-003	1.236
80	1.1412E-003	1.344	9.2667E-004	2.076
160	2.5398E-004	2.167	1.2164E-004	2.929
320	9.6087E-005	1.402	1.0321E-004	0.237

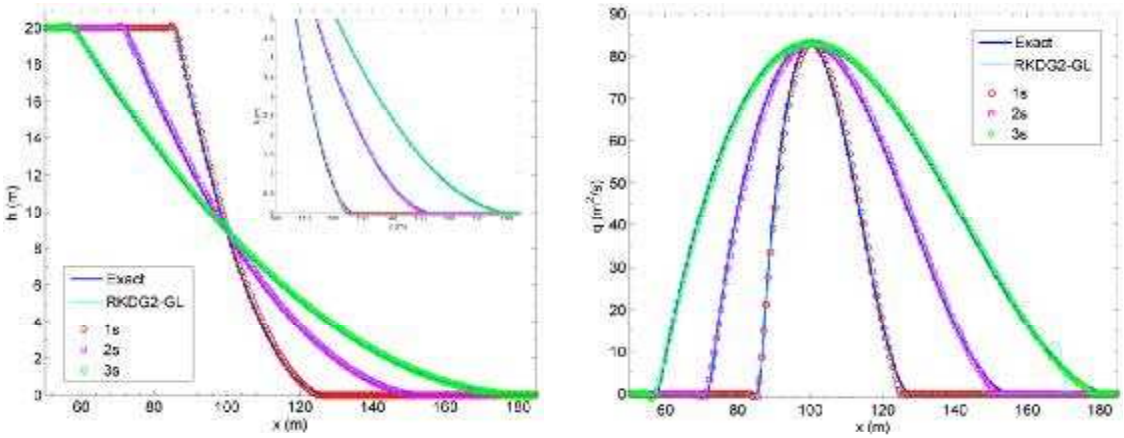

Fig. 5: RKDG2 solutions to the Riemann problem at different output times (N = 320). Sub-case 2: dam-break flow.

The second sub-case can be viewed as an idealized dam-break flow in a 200m long channel. The dam is initially located at x = 100m and splits the domain into an upstream reservoir with h = 20m and q = 0m^2/s and a downstream dry zone. The dam is removed at t = 0s to produce a wet/dry front propagating towards the downstream and a depression wave moving upstream. Simulation is run on a uniform grid with 320 cells with transmissive boundary conditions imposed at both ends. Fig. 5 compares the RKDG2 profiles with the exact solutions at t = 1, 2 and 3s. The RKDG2-LL is found to trail correctly the moving wet/dry front and provide superior results than the RKDG2-GL. The GL tends to develop numerical discrepancies around the wet/dry front and a small amount of artificial viscosity at the point of transcritical flow. Furthermore, inaccurate prediction near the wet/dry front seems to grow in time and the scheme clearly fails at t = 3s as seen from the zoom-in graph for depth profiles and from the discharge plots in Fig. 5.

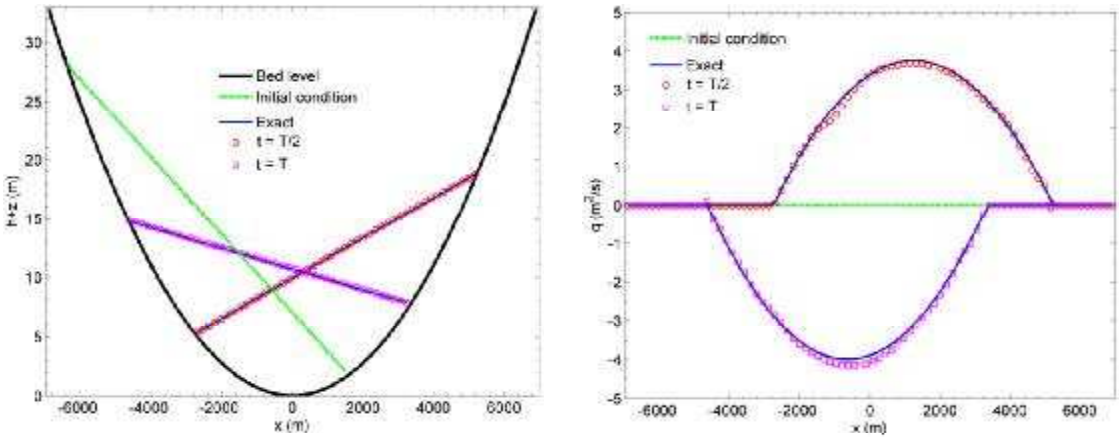

Fig. 6: Oscillatory lake with friction effects: RKDG2-LL flow profiles at $t = T / 2$ and T.

4.3. Oscillatory lake with friction effects

This is a numerically challenging test as it involves constantly moving wet/dry interfaces and non-uniform bed topography. It consists of an oscillatory frictional flow taking place in a parabolic bowl [46]. The topography follows $z(x) = h_0 (x/a)^2$ with h_0 and a being constants. Sampson [43] derived an analytical solution for this case by assuming a friction source term that is proportional to the discharge, *i.e.* $S_f = -\tau q$ (τ is a constant friction factor). The resulting analytical solution is provided as follows

$$\eta(x,t) = h_0 + \frac{a^2 B^2 e^{-\tau t}}{8g^2 h_0}\left(-s\tau \sin 2st + (\tau^2/4 - s^2)\cos 2st\right) - \frac{B^2 e^{-\tau t}}{4g} - \frac{e^{-\tau t/2}}{g}\left(Bs\cos st + \frac{\tau B}{2}\sin st\right)x \tag{56}$$

$$u(x,t) = Be^{-\tau t/2}\sin 2st \tag{57}$$

where B is a constant and $s = \sqrt{8gh_0 - \tau^2}\,/\,2a$.

Table 3a: L^1–Error and order of accuracy at $t = T/2$: Oscillatory lake with friction effects.

No. of cells (N)	$h+z$ (m)		q (m^2/s)	
	L^1–Errors	L^1–Rate	L^1–Errors	L^1–Rate
20	4.8864E-003	--	1.7465E-002	--
40	1.2299E-003	1.990	6.2412E-003	1.484
80	3.0233E-004	2.024	1.0300E-003	2.599
160	7.2931E-005	2.051	2.7507E-004	1.904

320	1.7099E-005	2.092	6.5803E-005	2.063

Table 3b: L^{∞}–Error and order of accuracy at $t = T/2$: Oscillatory lake with friction effects.

No. of cells (N)				
	$h + z$ (m)		q (m^2/s)	
	L^{∞}–Errors	L^{∞}–Rate	L^{∞}–Errors	L^{∞}–Rate
20	4.8055E-003	--	2.8261E-002	--
40	1.2011E-003	2.000	1.0329E-002	1.452
80	3.0209E-004	1.991	1.2123E-003	3.090
160	7.3878E-005	2.031	3.1901E-004	1.926
320	1.7371E-005	2.088	7.1725E-005	2.153

Table 4a: L^{1}–Error and order of accuracy at $t = T$: Oscillatory lake with friction effects.

No. of cells (N)				
	$h + z$ (m)		q (m^2/s)	
	L^{1}–Errors	L^{1}–Rate	L^{1}–Errors	L^{1}–Rate
20	3.7959E-003	--	2.4616E-002	--
40	9.5017E-004	1.998	7.1438E-003	1.784
80	2.3856E-004	1.993	1.6605E-003	2.105
160	5.8005E-005	2.040	3.9117E-004	2.085
320	1.3592E-005	2.093	9.5121E-005	2.040

Table 4b: L^{∞}–Error and order of accuracy at $t = T$: Oscillatory lake with friction effects.

No. of cells (N)				
	$h + z$ (m)		q (m^2/s)	
	L^{∞}–Errors	L^{∞}–Rate	L^{∞}–Errors	L^{∞}–Rate
20	4.8012E-003	--	2.9146E-002	--
40	1.2011E-003	2.002	7.4763E-003	1.962
80	3.0222E-004	1.990	1.8397E-003	2.022
160	7.3878E-005	2.032	4.6471E-004	1.985
320	1.7371E-005	2.088	1.1504E-005	2.014

The computational domain is chosen to be [–7000m; 7000m] and the constants are set so that a = 4000m, h_0 = 11m, and B = 9m/s. If $\tau = 0$, the flow is frictionless and oscillates indefinitely in the domain with a period of T = 1711s [46]. By setting $\tau = 0.0015\text{s}^{-1}$, the oscillatory flow decays with time until the motionless steady state is reached (i.e. $\eta(x,\infty) = h_0$ and $q(x,\infty) = 0$). With transmissive boundary conditions, the flow is simulated for 18 oscillating periods on a uniform grid of 80 cells. Fig. 6 illustrates the initial flow conditions and the RKDG2-LL numerical results at $t = T/2$ and $t = T$. The final motionless steady state at $t = 18T$ is presented separately in Fig. 7. At all of the output times, the numerical predictions agree excellently with the analytical solutions. As seen clearly from

Fig. 6 and Fig. 7, the present method ensures better momentum conservation where the time evolving discharge profile follows closely the analytical solution. The mass error has also been recorded for the entire simulation until $t = 18T$. Its magnitude maintains at a scale equivalent to the machine precision error and so it is not illustrated herein. In this case, RKDG2-GL predicts similar results as RKDG2-LL does because the flow does not contain solution with sharp gradients. Therefore, the RKDG2-GL predictions are not presented.

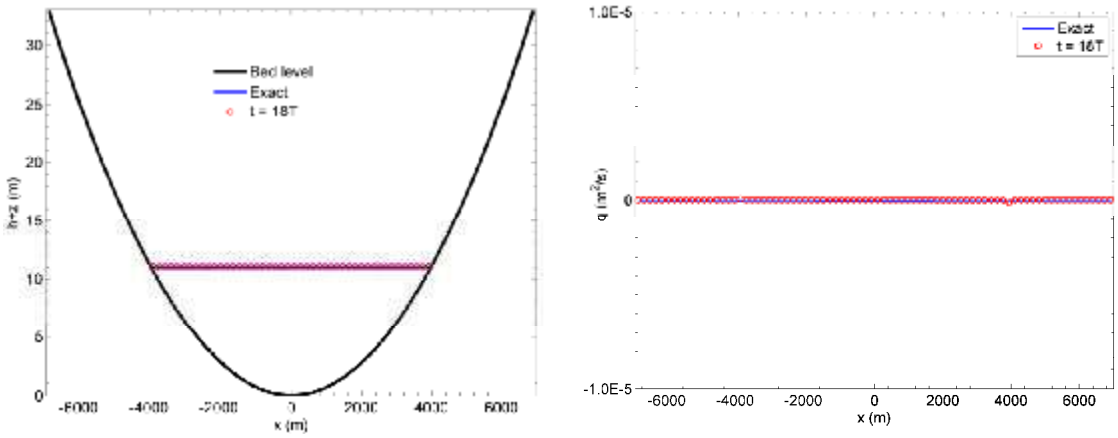

Fig. 7: Oscillatory lake with friction effects: RKDG2-LL predicted motionless steady state at $t = 18T$.

Table 3 and 4 list the error and order of accuracy computed at $t = T/2$ and $t = T$ that are obtained by running a series of simulations on different grids as in the pervious test. It is evident from Table 3 and Table 4 that the present RKDG2-LL scheme is again able to reach second-order accuracy for both flow variables. Specifically, this test involves wetting and drying as well as non-zero source terms for both topography and friction. This indicates that the proposed splitting implicit discretization approach for friction terms and the wetting and drying treatment do not affect the overall second-order accuracy of the numerical scheme as well as the momentum conservation.

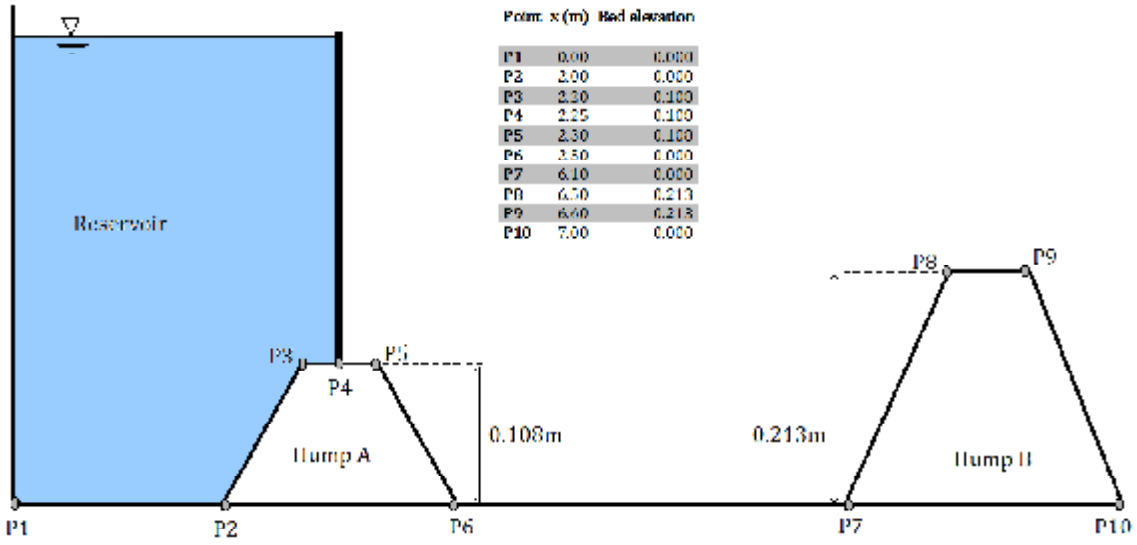

Point	x (m)	Bed elevation
P1	0.00	0.000
P2	3.00	0.000
P3	3.20	0.108
P4	3.25	0.108
P5	3.30	0.108
P6	3.50	0.000
P7	6.10	0.000
P8	6.50	0.213
P9	6.60	0.213
P10	7.00	0.000

Fig. 8: Experimental setup for the frictional dam-break flow over two humps.

4.4. Dam-break flow over two frictional humps

The dam-break experimental benchmark provided by Aureli et al. [5] is employed herein to further demonstrate the performance of the current RKDG2 models. This test case simultaneously includes most of the challenging features that a numerical scheme may encounter when coping with a real-world flood simulation, e.g. propagating bores and reflection waves, surface curvatures, repeatedly wetting and drying, non-differentiable topography, high roughness value and steady-state equilibrium.

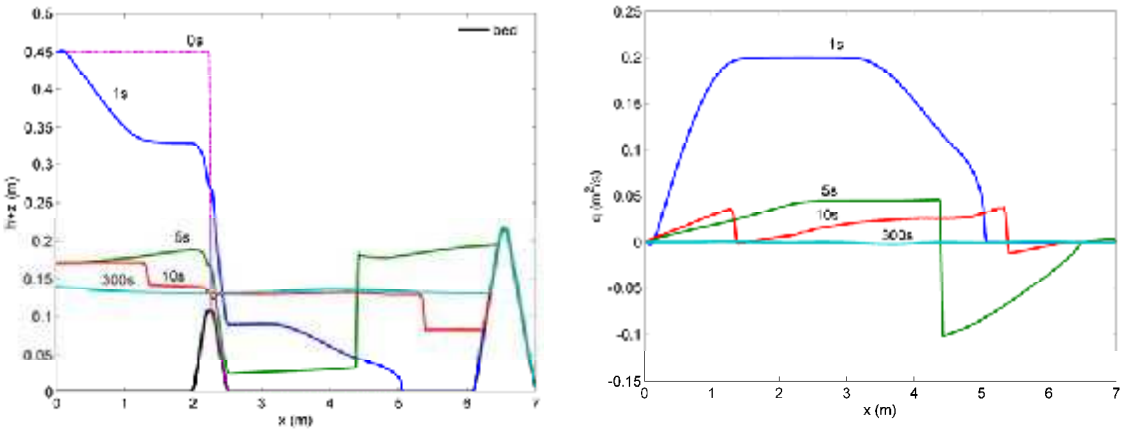

Fig. 9: RKDG2-LL predicted flow profiles at different output times for the dam-break flow over two humps with friction effects.

The domain is 7m long and involves two humps (hump A and hump B) as indicated in Fig. 8. The dam is built on the top of hump A and hump B is located right before the downstream end of domain. Upstream of the dam, the still water level is 0.342m and the downstream floodplain is initially dry. A constant Manning coefficient of 0.01 is assumed. The upstream boundary is closed while a free outflow is assumed at the downstream end. The simulation is first run on a grid with $N = 300$ cells and for $t = 300$s after the dam fails. Fig. 9 provides flow profiles in terms of free-surface elevation and discharge predicted by RKDG2-LL at $t = 0$s, 1s, 5s, 10s, and 300s. The wet/dry front and the flood wave interactions with the two obstacles are reasonably well-modelled and the expected steady state is nearly reached at $t = 300$s.

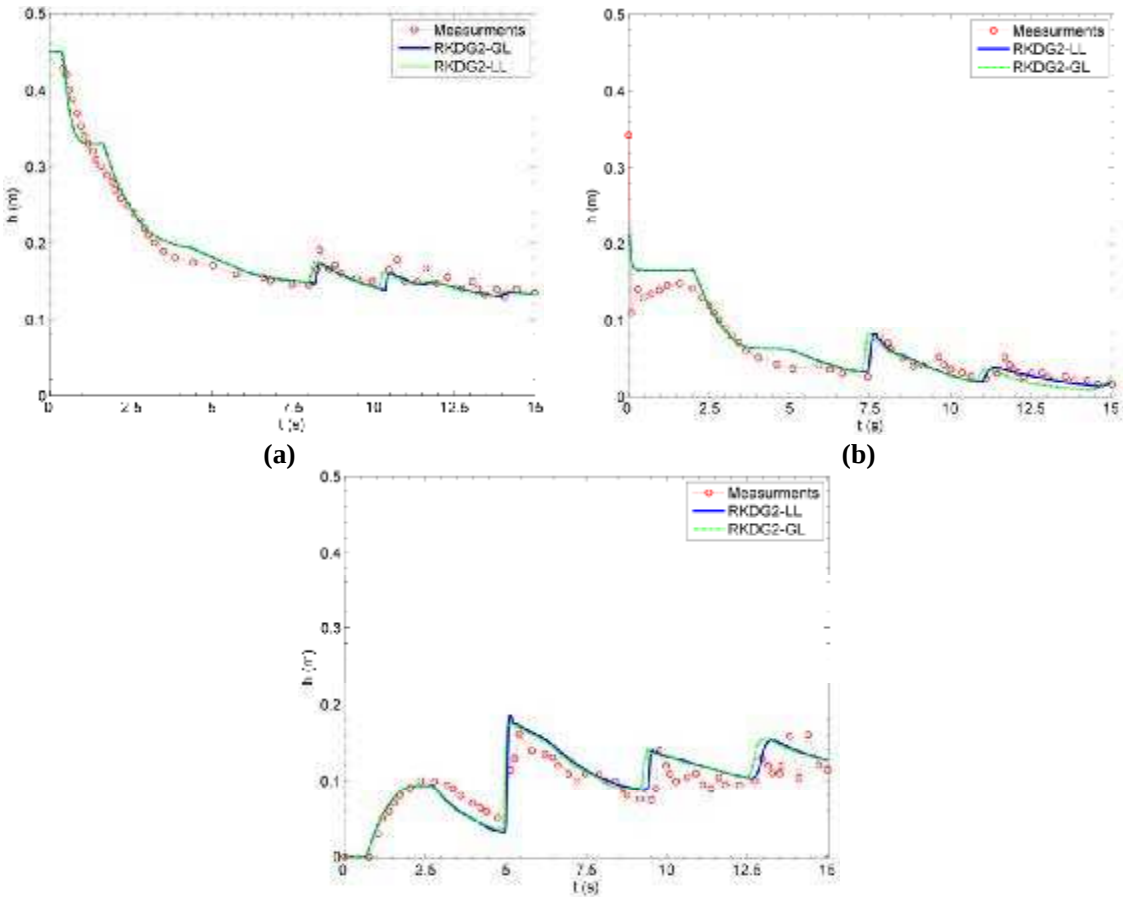

Fig. 10: RKDG2-LL and RKDG2-GL predicted time histories of the water depth at $x = 1.4$m, 2.25m and 4.5m, compared with the experimental data.

A second simulation is then launched up to 15s and in line with the grid used in [5] (i.e. N = 144 cells). Fig. 10 presents the time evolution of water depth at three gauge points located at x = 1.4m, 2.25m and 4.5m and compares the numerical predictions with the experimental data. At all of the gauges, the results computed by both RKDG2-LL and RKDG2-GL compare reasonably well with the experimental data. However, the RKDG2-GL is observed to slightly delay the arrival time of the flood wave. Compared further with the alternative finite volume results available in [5], the RKDG2-LL seems to predict arrival times closer to the experimental data.

5. Summary and conclusions

A new well-balanced RKDG2 numerical model has been developed to include wetting and drying over irregular topography. An FV non-negative reconstruction technique has been used to rebuild the Riemann states for calculating the HLL inter-cell fluxes. New amendments have been proposed to regenerate the coefficients defining the local approximate linear solution and topography in accordance with the *positivity-preserving* Riemann states for flux and source term calculations. These measures do not impose any additional restriction on the time step and are found to essentially maintain the well-balanced property, non-negativity of water depth and conservation of mass and momentum in the context of an RKDG2 scheme. The friction terms are separately discretized by a splitting implicit approach, which also accounts for the RKDG2 local slope coefficients.

Another focus of this work is to resolve the issue related to slope limiting. For this purpose, both global and local slope limiting processes have been implemented in the proposed RKDG2 model (RKDG2-GL and RKDG2-LL). Intensive numerical experiments have been carried out to reveal the advantages and drawbacks of the limiters. Overall, the RKDG2-GL scheme tends to produce less accurate or even misleading numerical solutions

for certain test cases, especially those tests involving sharp gradients of flow variables. In contrast, the RKDG2-LL scheme delivers more accurate and reliable predictions for most of the complicated flow patterns relevant to realistic flood simulations. The RKDG2-LL scheme is also observed to better maintain momentum conservation and therefore has better potential in practical simulations.

Acknowledgement

This work is funded by the UK Engineering and Physical Sciences Research Council (EPSRC) through grant: EP/F030177/1.

References

1. Aizinger V, Dawson C. A discontinuous Galerkin method for two-dimensional flow and transport in shallow water. Adv Wat Res 2002; 25(1):67–84.
2. Ambati VR, Bokhove O. Space–time discontinuous Galerkin discretization of rotating shallow water equations. J Comput Phys 2007; 225(2):1233–1261
3. Audusse E, Bouchut F, Bristeau MO, Klein R, Perthame B. A fast and stable well-balanced scheme with hydrostatic reconstruction for shallow water flows. SIAM J Sci Comput 2004; 25(6):2050–2065.
4. Aureli F, Maranzoni A, Mignosa P, Ziveri C. A weighted surface-depth gradient method for the numerical integration of the 2D shallow water equations with topography. Adv Wat Res 2008; 31(7):962–974.
5. Aureli F, Mignosa P, Tomirotti M. Dam-break flows in presence of abrupt bottom variations, Proc XXVIII IAHR Congr, Graz, Australia 1999, pp. 163–171.
6. Begnudelli L, Sanders BF. Conservative wetting and drying methodology for

quadrilateral grid finite-volume models. J. Hydr Engrg 2007; 133(3):312–322.

7. Bokhove O. Flooding and drying in discontinuous Galerkin finite element method for shallow water flows. J Sci Comput 2005; 22-23(1):47–82.
8. Bradford SF, Sanders BF. Finite volume model for shallow water flooding of arbitrary topography. J Hydr Engrg 2002; 128(3):289–298.
9. Brufau P, García-Navarro P, Vázquez-Cendón ME. Zero mass error using unsteady wetting-drying conditions in shallow flows over dry irregular topography. Int J Numer Meth Fluids 2004; 45(10):1047–1082.
10. Bunya S, Kubatko EJ, Westerink JJ, Dawson C. A wetting and drying treatment for the Runge-Kutta discontinuous Galerkin solution to the shallow water equations. Comput Meth Appl Mech Engrg 2009; 198(17-20):1548–1562.
11. Burguete J, García-Navarro P, Murillo J, García-Palacín I. Analysis of the friction term in the one-dimensional shallow water model. J Hydr Engrg 2007; 133(9):1048–1063.
12. Burguete J, García-Navarro P, Murillo J. Friction term discretization and limitation to preserve stability and conservation in the 1D shallow-water model: Application to unsteady irrigation and river flow. Int J Numer Meth Fluids 2008; 58(4):403–425.
13. Castro-Díaz MJ, Fernández-Nieto ED, Ferreiro AM, Parés C. Two-dimensional sediment transport models in shallow water equations. A second order finite volume approach on unstructured meshes. Comput Meth App Meth Eng 2009; 198(33-36):2520–2538.
14. Casulli V. A high-resolution wetting and drying algorithm for free-surface hydrodynamics. Int J Numer Meth Fluids 2009; 60(4):391–408.
15. Cockburn B, Shu CW. Runge-Kutta discontinuous Galerkin methods for convection-dominated problems. J Sci Comput 2001; 16(3):173–261.
16. Cockburn B, Shu CW. The Runge-Kutta local projection P1-discontinuous Galerkin method for scalar conservation laws. RAIRO Modél Math Anal Numér 1991; 25(3):337–

361.

17. Ern A, Piperno S, Djadel K. A well-balanced Runge-Kutta discontinuous Galerkin method for the shallow-water equations with flooding and drying. Int J Numer Meth Fluids 2008; 58(1):1–25.
18. Eskilsson C, Sherwin SJ. A triangular spectral/hp discontinuous Galerkin method for modelling 2D shallow water equations. Int J Numer Meth Fluids 2004; 45(6):605–623.
19. Fagherazzi S, Rasetarinera P, Hussaini YM, Furbish DJ. Numerical solution of the dam-break problem with a discontinuous Galerkin method. J Hydr Engrg 2004; 130(6):532–539.
20. Gallardo JM, Parés C, Castro M. On a well-balanced high-order finite volume scheme for shallow water equations with topography and dry areas. J Comput Phys 2007; 227(1):574–601.
21. Gallouët T, Hérard JM, Seguin N. Some approximate Godunov schemes to compute shallow-water equations with topography, Comput Fluids 2003; 32(4):479–513.
22. Giraldo FX, Warburton T. A high-order triangular discontinuous Galerkin oceanic shallow water model. Int J Numer Meth Fluids 2008; 56(7):899–925.
23. Giraldo FX. High-order triangle-based discontinuous Galerkin methods for hyperbolic equations on a rotating sphere. J Comput Phys 2006; 214(2):447–465.
24. Gourgue O, Comblen R, Lambrechts J, Kärnä T, Legat V, Deleersnijder E. A flux-limiting wetting–drying for finite element shallow-water models, with application to Scheldt Estuary. Adv Wat Res 2009; 32(12):1726–1739.
25. Guinot V. Godunov-type schemes: an introduction for engineers. Elsevier: Amsterdam, 2003.
26. Hubbard ME, Dodd N. A 2D numerical model of wave run-up and overtopping. Coast Engrg 2002; 47(1):1–26.

27. Kesserwani G, Ghostine R, Vazquez J, Ghenaim A, Mosé R. Application of a second-order Runge-Kutta discontinuous Galerkin scheme for the shallow water equations with source terms. Int J Numer Meth Fluids 2008; 56(7):805-821.
28. Kesserwani G, Liang Q, Vazquez J, Mosé R. Well-balancing issues related to the RKDG2 scheme for the shallow water equations. Int J Numer Meth Fluids 2010; 62(4)428–448.
29. Krivodonova L, Xin J, Remacle JF, Chevaugeon N, Flaherty JE. Shock detection and limiting with discontinuous Galerkin methods for hyperbolic conservation laws. Appl Numer Math 2004; 48(3-4);323–338.
30. Kubatko EJ, Bunya S, Dawson C, Westerink JJ, Mirabito C. A performance comparison of continuous and discontinuous finite element shallow water models. J Sci Comput 2009; 40(1-3):315-339.
31. Kubatko EJ, Bunya S, Dawson C, Westerink JJ. Dynamic p-adaptive Runge–Kutta discontinuous Galerkin methods for the shallow water equations. Comput Meth App Mech Engrg 2009; 198(21-26):1766–1774.
32. Kubatko EJ, Westerink JJ, Dawson C. Hp Discontinuous Galerkin methods for advection dominated problems in shallow water flow. Comput Meth App Meth Eng 2006; 96(1-3):437–451.
33. Lee SH, Wright NG. A simple and efficient solution of the shallow water equations with source terms. Int J Numer Meth Fluids 2010; 63(3):313–340.
34. Liang Q, Borthwick AGL. Adaptive quadtree simulation of shallow flows with wet–dry fronts over complex topography. Comput Fluids 2009; 38(2):221–234.
35. Liang Q, Marche F. Numerical resolution of well-balanced shallow water equations with complex source terms. Adv Wat Res 2009; 32: 873–884.
36. Liang Q. Flood simulation using a well-balanced shallow flow model. ASCE-J Hydr

Engrg 2010; doi:10.1061/(ASCE)HY.1943-7900.0000219.

37. Marche F, Bonneton P, Fabrie P, Seguin N. Evaluation of well-balanced bore-capturing schemes for 2D wetting and drying processes. Int J Numer Meth Fluids 2007; 53(5):867–894.
38. Murillo J, García-Navarro P, Burguete J. Time step restrictions for well-balanced shallow water solutions in non-zero velocity steady states. Int J Numer Meth Fluids 2009; 60(12):1351–1377.
39. Nair RD, Thomas SJ, Loft RD. A discontinuous Galerkin global shallow water model. Mon Weather Rev 2005; 133(4):876–888.
40. Nikolos IK, Delis AI. An unstructured node-centred finite volume scheme for shallow water flows with wet/dry fronts over complex topography. Comput Meth App Mech Eng 2009; 189(47-48):3723–3750.
41. Qiu J, Shu CW. A comparison of troubled-cell indicators for Runge-Kutta Discontinuous Galerkin methods using weighted essentially nonoscillatory limiters. SIAM J Sci Comput 2005; 27(3):995–1013.
42. Remacle JF, Soares-Frazão S, Li X, Shephard MS. An adaptive discretization of the shallow water equations based on discontinuous Galerkin methods. Int J Numer Meth Fluids 2006; 52(8):903–923.
43. Sampson S. A numerical solution for moving boundary shallow water flow above parabolic bottom topography. ANZIAM J 2009; 50(CTAC2008):C898–C911.
44. Schwanenberg D. Die Runge-Kutta-Discontinuous-Galerkin-Methode zur Lösung konvektionsdominierter tiefengemittelter Flachwasserprobleme. PhD thesis; Fakultät für Bauingenieurwesen, 2003.
45. Sobey RJ. Wetting and drying in coastal flows. Coast Engrg 2009; 56(5-6):565–576.
46. Thacker WC. Some exact solutions to the nonlinear shallow-water wave equations. J

Fluid Mech 1981; 107:499–508.

47. Toro EF, García-Navarro P. Godunov-type methods for free-surface shallow flows: A review. J Hydr Res 2007; 45(6):737–751.
48. Toro EF. Shock-capturing methods for free-surface shallow flows. John Wiley & Sons, Ltd, 2001.
49. Van Leer B. Upwind high-resolution methods for compressible flow: From donor cell to residual-distribution schemes. Commun Comput Phys 2006; 1(2):192–206.
50. Xing Y, Shu CW. A new approach of high order well-balanced finite volume WENO schemes and discontinuous Galerkin methods for a class of hyperbolic systems with source terms. Commun Comput Phys 2006; 1(1):101–135.
51. Xing Y, Shu CW. High order well-balanced finite volume WENO schemes and discontinuous Galerkin methods for a class of hyperbolic systems with source terms. J Comput Phys 2006; 214(2):567–598
52. Zhao DH, Shen HW, Tabios GQ, Lai JS, Tan WY. Finite volume two-dimensional unsteady flow model for river basins. J Hydr Engrg 1994; 120(7):863–883.
53. Zhou T, Li Y, Shu CW. Numerical Comparison of WENO Finite Volume and Runge–Kutta Discontinuous Galerkin Methods. J Sci Comput 2001; 16(2):145–171.
54. Zokagoa J-M, Soulaïmani A. Modeling of wetting–drying transitions in free surface flows over complex topographies. Comput Meth Appl Mech Engrg 2010; 199(33-36):2281–2304.
55. Mungkasi S, Roberts SG. On the best quantity reconstructions for a well-balanced finite volume method used to solve the shallow water wave equations with a wet/dry interface. ANZIAM J. 51 (EMAC2009) 2010; C48–C65.